

Supporting Information

Proton Coordination Chemistry in Pyrene-based Anode for Ultralong-life Aqueous Proton Batteries

Wenhui Yang,^{a‡} Chensi Zhan,^{a‡} Qiang Zhu,^{b‡} Lei Liu,^a Baiming Su,^a Haoxiang Yu,^a Liyuan Zhang,^a Lei Yan,^{a*} Jie Shu^{a*}

^a School of Materials Science and Chemical Engineering, Ningbo University, Ningbo, Zhejiang, 315211, China

^b Molecular Horizons and School of Chemistry and Molecular Bioscience, University of Wollongong, NSW 2522, Australia

*Corresponding author: Lei Yan

E-mail: yanlei@nbu.edu.cn

*Corresponding author: Jie Shu

E-mail: shujie@nbu.edu.cn

‡These authors contributed equally to this work.

Experimental Procedures

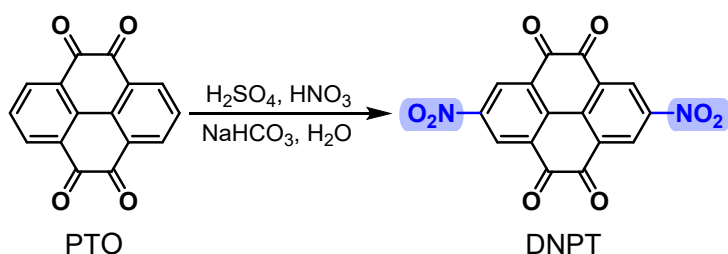
Materials

Pyrene-4, 5, 9, 10-tetraone (PTO, $\geq 98\%$) was purchased from Shanghai Aladdin Biochemical Technology Co., Ltd. Nitric acid (HNO_3 , analytical reagent) was purchased from Zhejiang Zhongxing Chemical Reagent Co., Ltd. Sulfuric acid (H_2SO_4 , analytic reagent) was purchased from Huzhou Shuanglin Chemical Technology Co., Ltd. Sodium bicarbonate (NaHCO_3 , 99%) was purchased from 3A Chemicals. Phosphoric acid (H_3PO_4 , analytical reagent) was purchased from Sinopharm Chemical Reagent Co., Ltd. Ketjen black (KB, ECP600JD) was purchased from Suzhou Siner Technology Co., Ltd. Activated carbon (AC, pharmaceutical grade) and polytetrafluoroethylene preparation (PTFE, 60 wt.%) were purchased from Shanghai Macklin Biochemical Co., Ltd. None of the reagents were further purified before usage.

Synthesis of 2, 7-dinitropyrene-4, 5, 9, 10-tetraone (DNPT)

In this research, DNPT was synthesized by nitration reaction according to the previously reported literatures,^{1, 2} as shown below (**Scheme S1**):

Initially, 20 mL $\text{H}_2\text{SO}_4/\text{HNO}_3$ mixed acid ($V_s:V_n=4:1$) was prepared. Then under stirring, PTO (2.10 mmol, 0.55 g) was added into the mixture to react at 90 °C. After 3 h of reaction, the resulting maroon solution was poured into 100 mL deionized (DI) water to form a suspension. Subsequently, the precipitate was collected by filtration and washed repeatedly with saturated NaHCO_3 and DI water. After vacuum drying at 65 °C for 24 h, yellow DNPT was obtained (0.64 g, 86.5% yield).



Scheme S1. Synthetic procedure of DNPT.

Material characterizations

The morphology and microstructure of synthesized DNPT sample were observed by scanning electron microscopy (SEM, FEI Nova NanoSEM 450) and transmission electron microscopy (TEM, FEI Tecnai F20, TF30). X-ray diffraction (XRD) patterns were carried out to grasp the structures of organic materials using a Bruker D8 Advance powder diffractometer equipped with Cu-K α radiation (40 mA, 40 kV) for 2θ ranging from 10 ° to 60 °. Thermogravimetric (TG, NETZSCH TG 209F3) data was collected under N₂ flow with a heating rate of 10 °C min⁻¹ from 25 °C to 900 °C. Raman spectrum of sample was detected by DXR3 Raman Microscope. Fourier transform infrared (FT-IR) spectra were measured by NICOLET 6700 in the range of 1000-4000 cm⁻¹ via KBr disk method. The surface chemical composition was analyzed by X-ray photoelectron spectroscopy (XPS, PerkinElmer PHI 550), and the charge correction value of C 1s was taken to be 284.8 eV. ¹H and ¹³C nuclear magnetic resonance (NMR) were performed in DMSO-*d*₆ on a 400 MHz NMR spectrometer (BRUKER AVANCE 400) to determine the structure of the prepared DNPT.

Electrochemical measurements

The DNPT working electrode was prepared by mixing DNPT, KB and PTFE in a weight ratio of 6:3:1, adding ethanol dropwise to the mixture and stirring continuously until a homogeneous slurry formed. Then the slurry was rolled into a film of uniform thickness and dried in vacuum at 60 °C overnight. The film was pressed onto Ti-mesh at the pressure of 20 MPa for 30 s to obtain the DNPT working electrode (1 cm², 1 mg_{DNPT} cm⁻²).

To prepare counter electrode, AC, acetylene black and PTFE were mixed in a weight ratio of 8:1:1. The preparation procedure was similar to that of DNPT working electrode whereas the mass loading of AC is ~6 mg cm⁻².

The electrochemical performance of the resultant electrodes was investigated based on typical three-electrode system, wherein Ag/AgCl electrode and 9.5 m H₃PO₄ solution served as reference electrode and electrolyte, respectively. Additionally, the volume of electrolyte used for battery fabricating is 10 mL in our work. Of note, during the discharge process from initial voltage to 0 V at a current density of 0.05 A g⁻¹, the nitro groups (-NO₂) were irreversibly reduced to amino groups (-NH₂) through a six-electron transfer reaction, which indicates the transformation from DNPT to PTO-NH₃⁺.³

Galvanostatic charge/discharge (GCD) profiles, long cycling stability, and galvanostatic intermittent titration technique (GITT) measurement were collected by using a multichannel battery test system (LAND CT2001A) in a voltage range of 0-1 V. Cyclic voltammetry (CV) and electrochemical impedance spectroscopy (EIS) tests were carried out on BioLogic VSP electrochemical workstation while the EIS data was at an open-circuit potential with a frequency range from 10 mHz to 100 kHz.

The ex-situ FTIR results were acquired with NICOLET 6700 FTIR Spectrometer while the ex-situ XPS results were obtained by PerkinElmer PHI 550. The batteries were assembled and pre-cycled at 1 A g⁻¹ for 25 cycles. After they were discharged/charged to corresponding potential, we washed the PTO-NH₃⁺ electrode with DI water for several times.

Electrochemical measurements analysis

(1) Specific capacity (C_m , mAh g⁻¹)

The specific capacity was calculated from GCD profiles according to the following equation:

$$C_m = \frac{I \times \Delta t}{3.6m} \quad (\text{Equation S1})$$

where I , Δt , and m denote the discharging current (A), discharging time (s) and mass loading (g) of active materials in working electrode, respectively.

(2) Capacitive contribution

Quantitative charge storage can be obtained based on the following equation:

$$i = av^b \quad (\text{Equation S2})$$

where i is the peak current (mA); v is the scan rate (mV s⁻¹); a and b represent adjustable parameters. If the b value is close to 0.5, revealing a diffusion-controlled reaction process; conversely, when b value approaches 1, the electrochemical process manifests as capacity-controlled.

To further improve the precision of reaction kinetics, the proportion of diffusion-controlled and capacity-controlled process can be calculated by the following equation:

$$i = k_1v + k_2v^{\frac{1}{2}} \quad (\text{Equation S3})$$

$$\frac{i}{v^2} = k_1 v^{\frac{1}{2}} + k_2 \quad (\text{Equation S4})$$

where i is the current (mA) at a specific potential; v is the scan rate (mV s⁻¹); k_1 and k_2 refer to constants, which can be attained from CV curves at different scan rates; $k_1 v$ and $k_2 v^{1/2}$ denote the capacity-contribution and diffusion-controlled contribution, respectively.

(3) GITT measurement

Before the GITT measurement, the three-electrode battery was first performed at 1 A g⁻¹ for 20 cycles to reach a stable state. Subsequently, a galvanostatic pulse (discharge or charge) with a current density of 0.1 A g⁻¹ was conducted for 5 min and then relaxed for 30 min to attain the equilibrium until the discharge (charge) potential reached 0 V (1.0 V) vs. Ag/AgCl. The diffusion coefficient (D_{ion}) can be calculated on the basis of the following equation:

$$D_{ion} = \frac{4}{\pi\tau} \left(\frac{m_B V_M}{M_B A} \right)^2 \left(\frac{\Delta E_s}{\Delta E_\tau} \right)^2 \quad (\text{Equation S5})$$

where τ , m_B , V_M , M_B , and A represent the duration time (s) of current pulse, mass loading (g) of active material, molar volume (cm³ mol⁻¹), molecular weight (g mol⁻¹) and contact area (cm²) between electrode and electrolyte, respectively. ΔE_s is the change of steady-state potential between two adjacent steps, while ΔE_τ is the total voltage change during each galvanostatic pulse procedure.

Computational details

All geometries we studied in this study were optimized with the help of Gaussian 16 package suite.⁴ Here, a hybrid density function, Becke three-parameter exchange and Lee-Yang-Parr correlation,⁵⁻⁷ augmented with Grimme's D3 dispersion correction,⁸ was employed. The def2-TZVP basis set was applied for C, H, O, and N atoms. The thermochemical data and local minima were later derived and confirmed by frequency estimation under the same method and basis set. The highest occupied molecular orbital (HOMO) and lowest unoccupied molecular orbital (LUMO) were later analyzed over optimized structures with the help of Multiwfn 3.8.⁹ The Gibbs energy changes were

estimated by the difference between the energies of complex (G_{PTO+nH^+}) and energies of isolated species ($\frac{1}{2}G_{H_2}, G_{PTO+(n-1)H^+}$), where G_{H_2} is the energy of H_2 molecule at vacuum.

Their corresponding mathematical expression is shown as below:

$$\Delta G = G_{PTO+nH^+} - \frac{1}{2}G_{H_2} - G_{PTO+(n-1)H^+} \quad (\text{Equation S6})$$

The charge density differences (CDD) were estimated by Multiwfn 3.8.⁹ All simulation visualizations were conducted by using Visual Molecular Dynamics (VMD).¹⁰

Supporting Figures, Discussions, and Tables

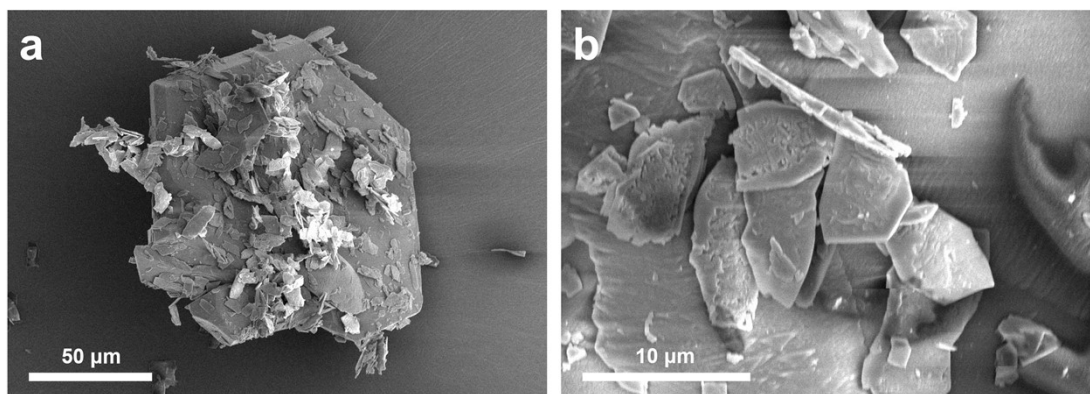


Fig. S1. SEM images of DNPT.

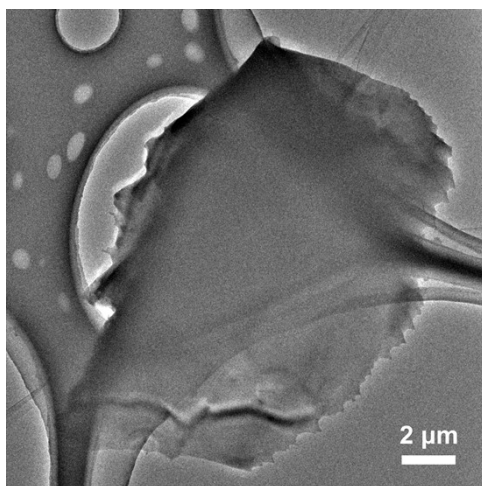


Fig. S2. TEM image of DNPT.

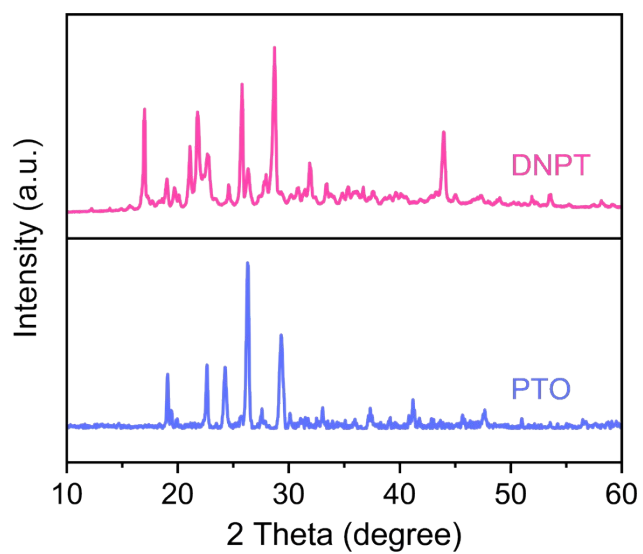


Fig. S3. XRD patterns of DNPT and PTO molecules.

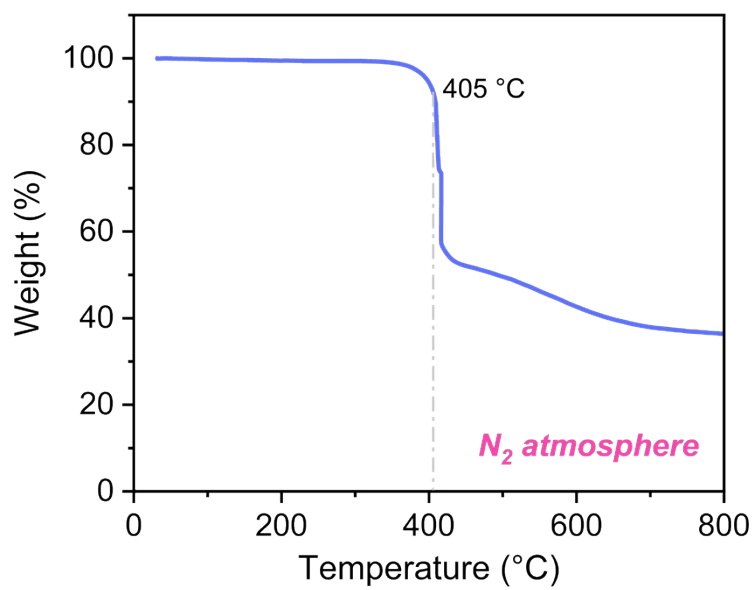


Fig. S4. Thermogravimetric analysis of DNPT (N_2 atmosphere, $5\text{ }^\circ\text{C min}^{-1}$).

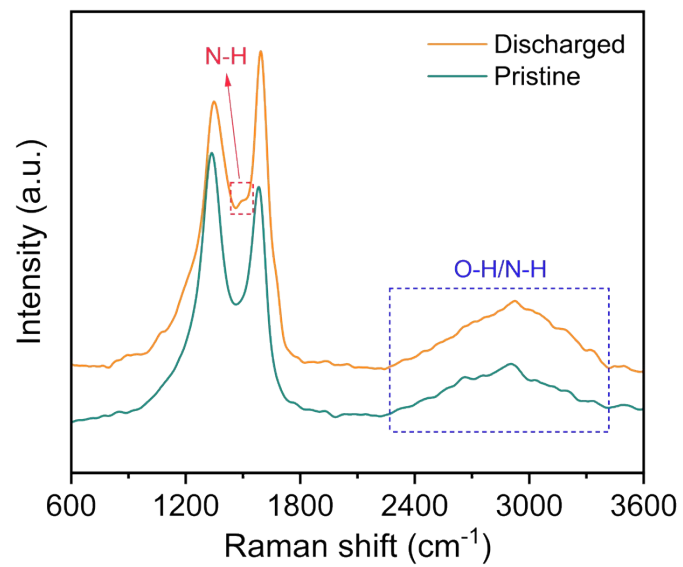


Fig. S5. Raman spectra of DNPT electrodes at different charge/discharge states.

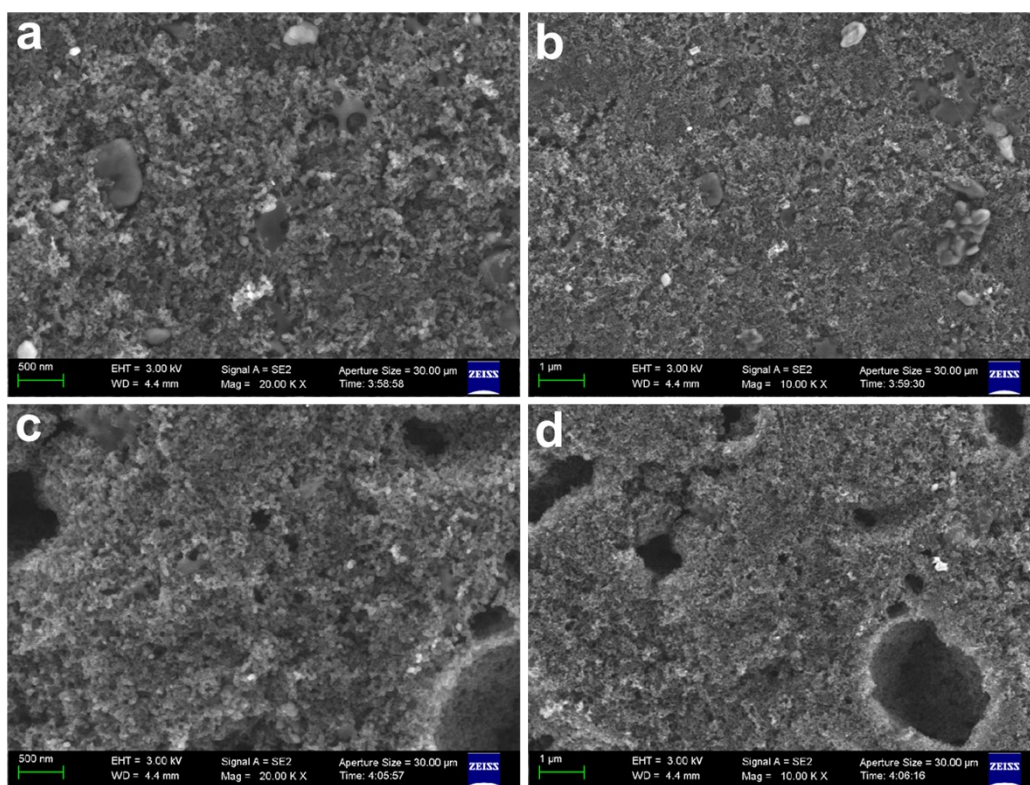


Fig. S6. SEM images of electrodes (a, b) before and (c, d) after electrochemical reduction.

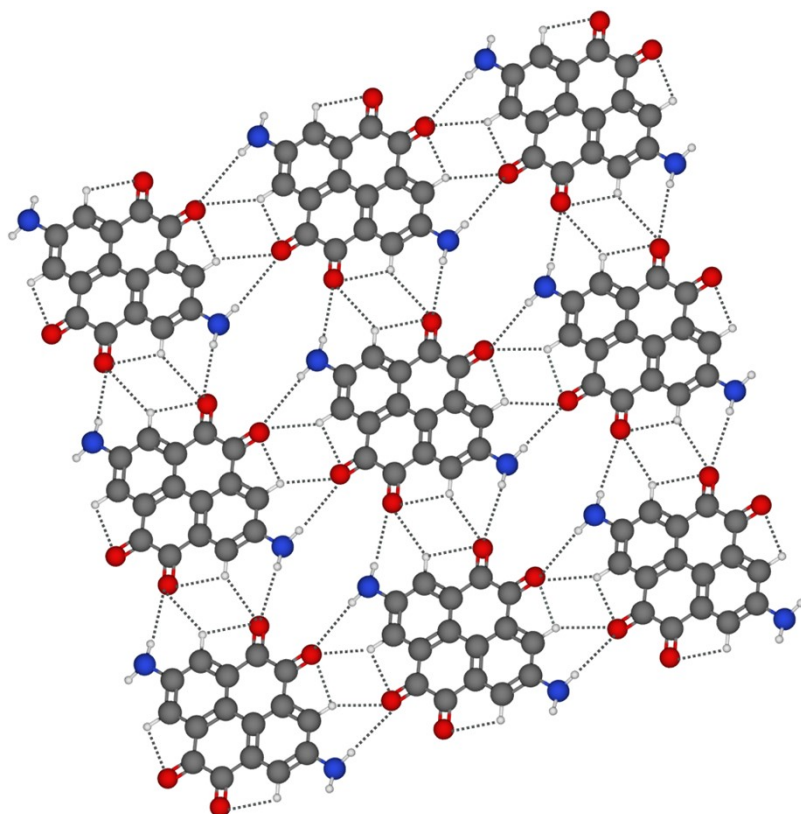


Fig. S7. The hydrogen bond networks structure of PTO-NH₂.

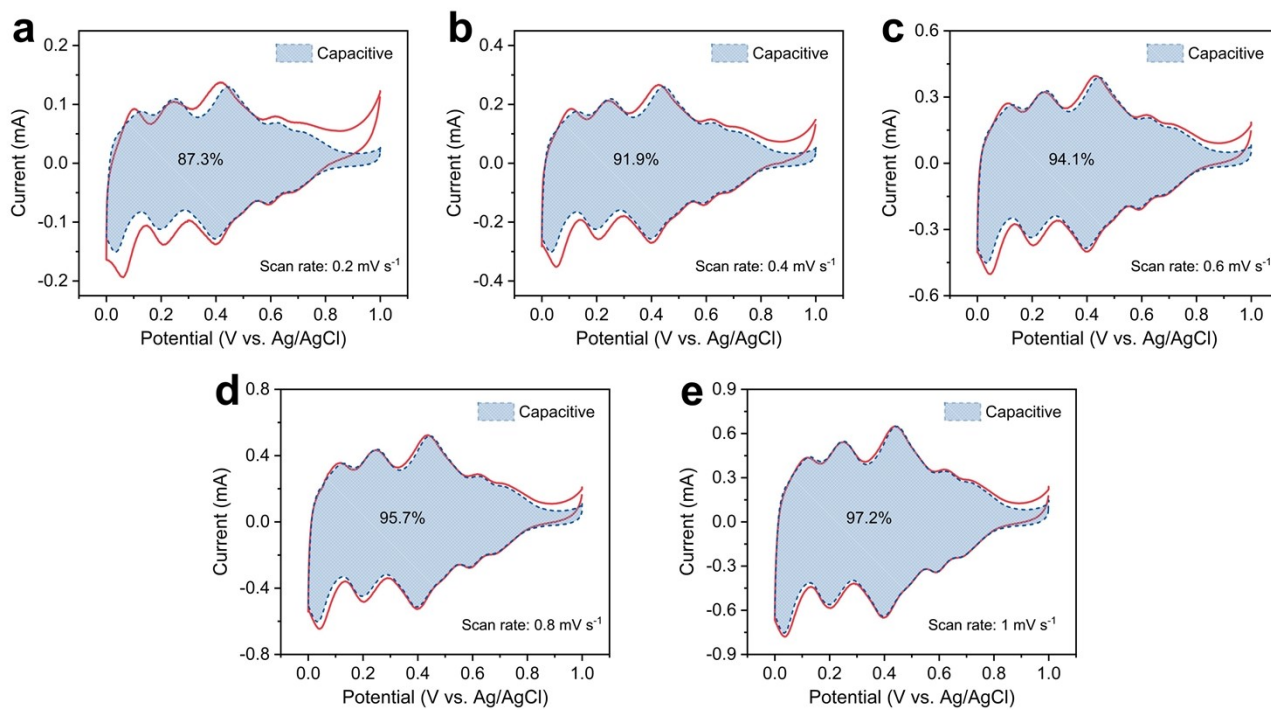


Fig. S8. Separation of the capacitive (shaded region) and diffusion currents at various scan rates of 0.2, 0.4, 0.6, 0.8, 1 mV s^{-1} .

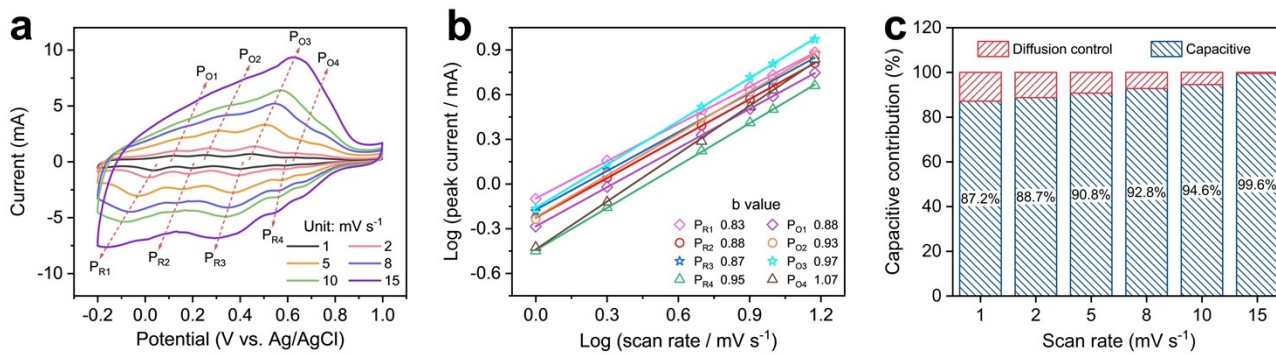


Fig. S9. (a) CV curves, (b) b values, and (c) capacitive contribution of PTO-NH₃⁺ electrode at various scan rates of 1, 2, 5, 8, 10, 15 mV s⁻¹ in aqueous 9.5 m H₃PO₄ electrolyte.

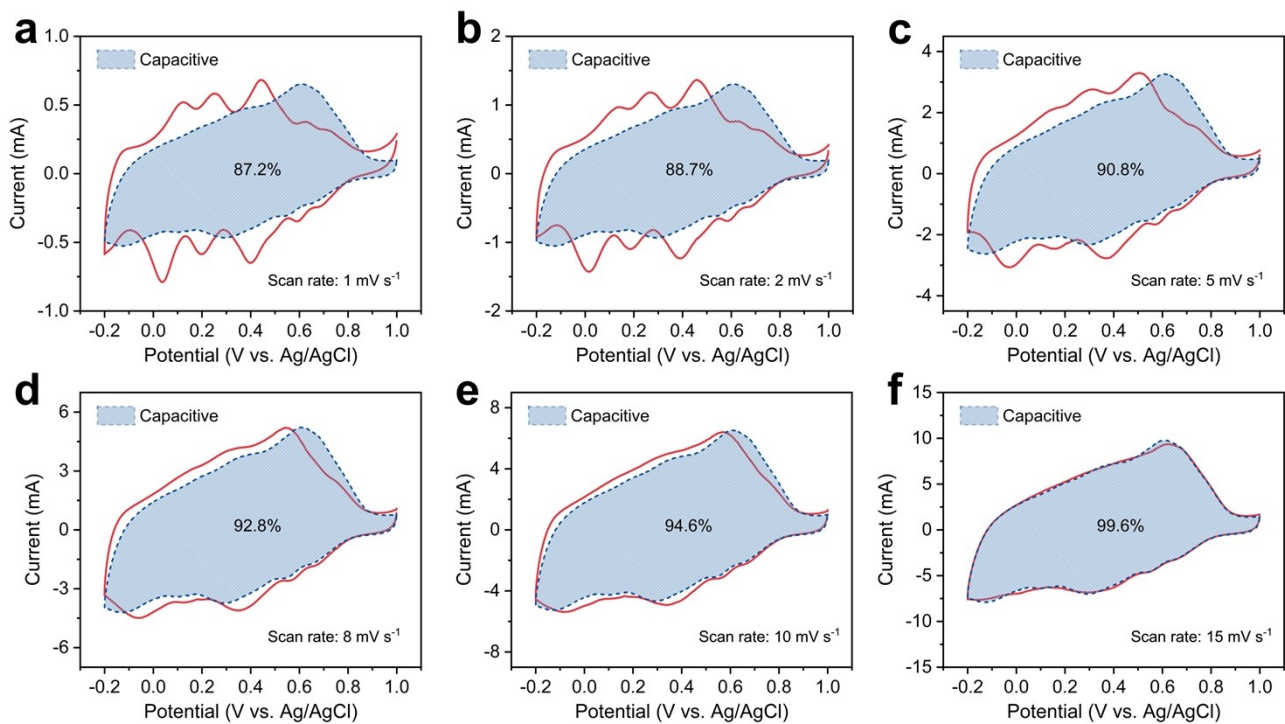


Fig. S10. Separation of the capacitive (shaded region) and diffusion currents at various scan rates of 1, 2, 5, 8, 10, 15 mV s^{-1} .

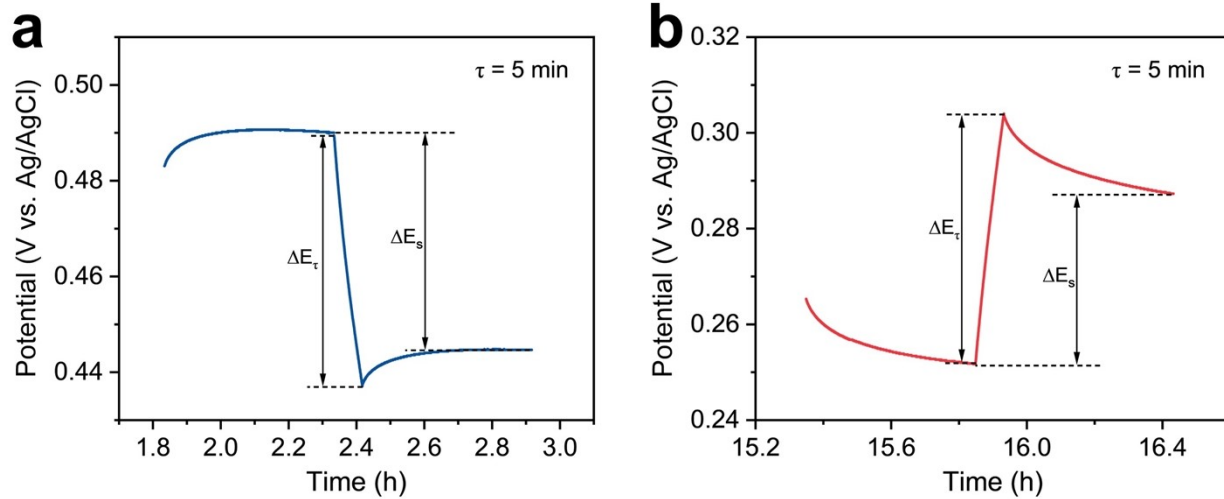


Fig. S11. Schematic illustration for selected steps of the GITT curves of PTO-NH₃⁺ electrode during discharge/charge process.

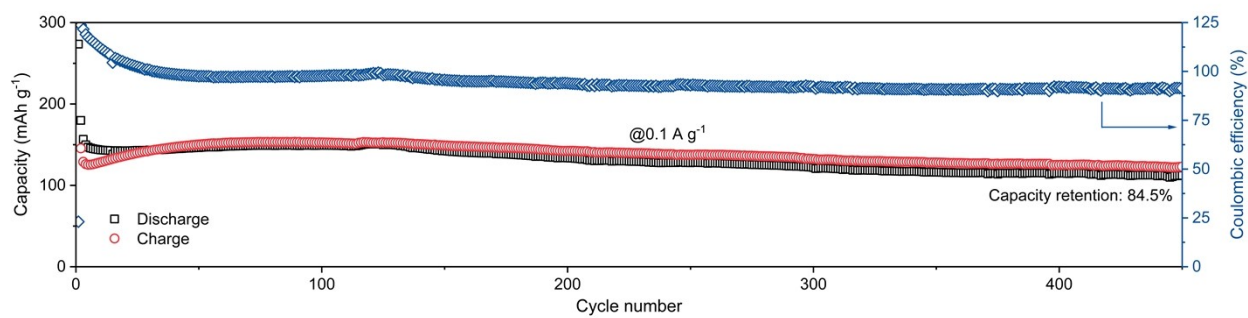


Fig. S12. Cycling performance of PTO-NH₃⁺ electrode at 0.1 A g⁻¹.

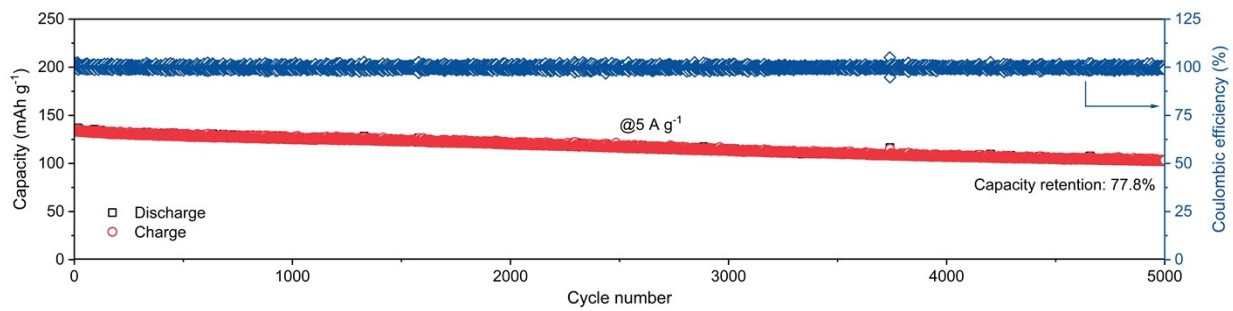


Fig. S13. Cycling performance of PTO-NH₃⁺ electrode at 5 A g⁻¹.

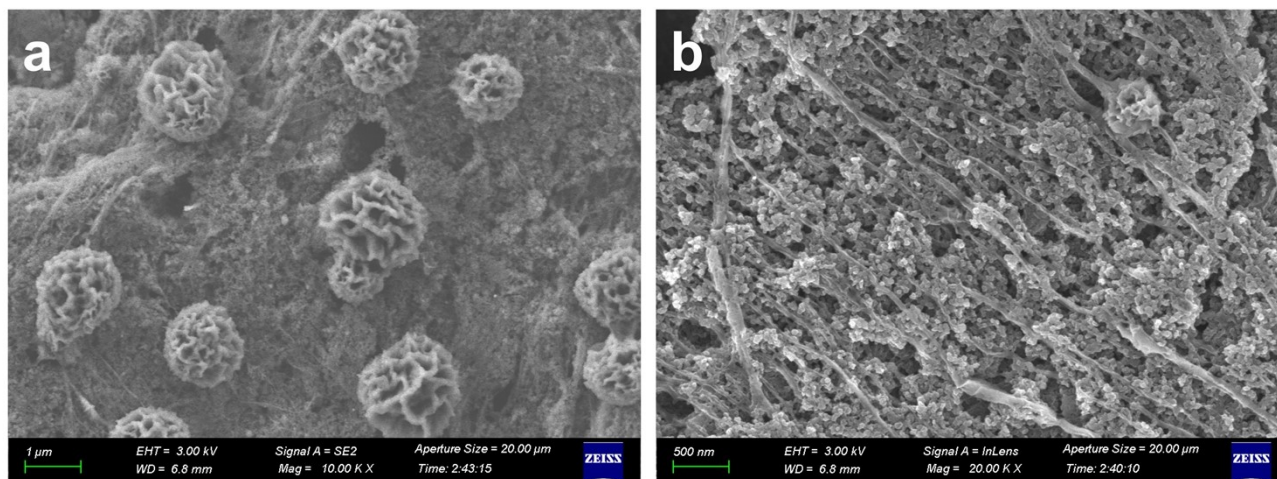


Fig. S14. SEM images of PTO-NH₃⁺ electrode after 10000 cycles.

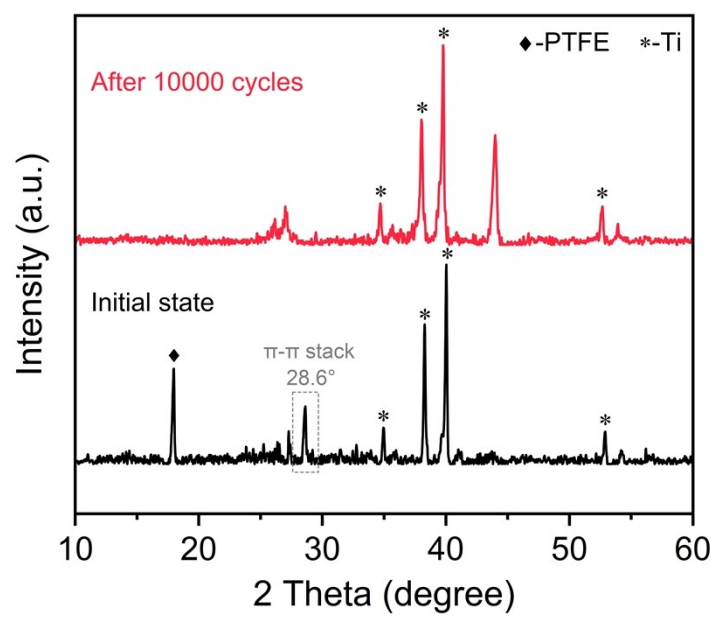


Fig. S15. XRD pattern of PTO-NH₃⁺ electrode after 10000 cycles.

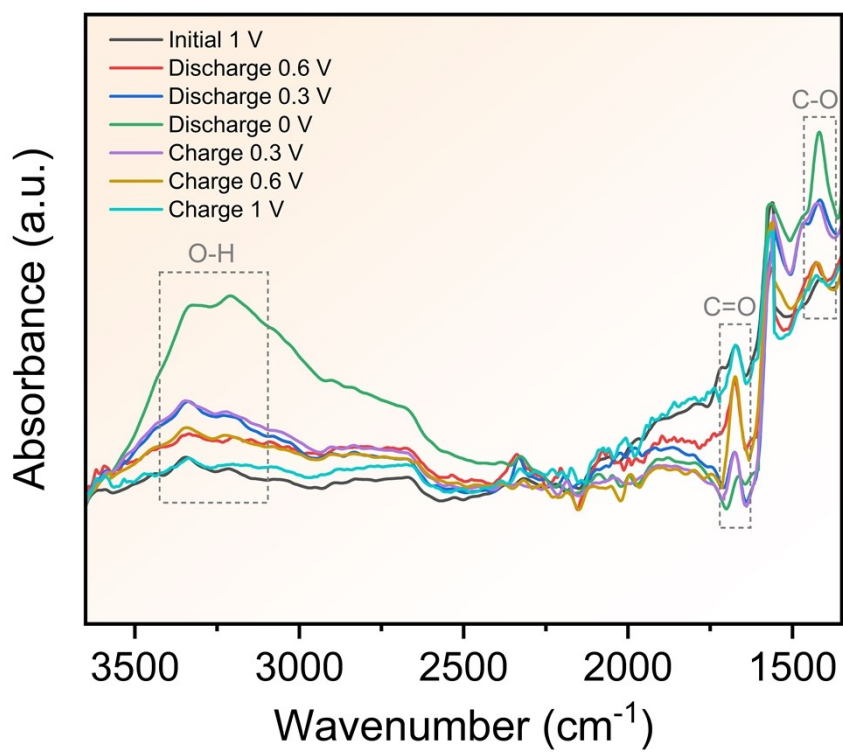


Fig. S16. Ex-situ FTIR spectra of PTO-NH₃⁺ electrodes at different charge/discharge states.

Table S1. Comparison of rate capacity of recently reported organic materials for aqueous proton batteries in the literatures.

References	Organic material	Electrolytes	Rate capacity (mAh g ⁻¹ , A g ⁻¹)	Cycling stability (capacity%; cycle number)
This work	PTO-NH₃⁺	9.5 m H₃PO₄	112.9, 40	74.1%; 10000
Ref. ¹¹	DPPZ	0.05 M H ₂ SO ₄	96.9, 15	95%; 400
Ref. ¹²	DPZ	1 M H ₂ SO ₄	145.9, 3	≈ 100%; 300
Ref. ¹³	PUQ	0.5 M H ₂ SO ₄	66.5, 20	82%; 1000
Ref. ¹³	PTC	0.5 M H ₂ SO ₄	62, 20	80%; 1000
Ref. ¹⁴	HATN	0.05 M H ₂ SO ₄ +0.2 M MnSO ₄	134, 20	≈ 100%; 2000
Ref. ¹⁵	PDPZ@MXene	2 M H ₂ SO ₄	161.3, 4	≈ 100%; 5000
Ref. ¹⁶	pDTP-AQ	1 M H ₂ SO ₄	58.9, 10.4	83%; 1000
Ref. ¹⁶	pDTP-NQ	1 M H ₂ SO ₄	56.5, 10.4	67%; 1000
Ref. ¹⁷	2, 6-DHN	0.5 M H ₂ SO ₄	81.9, 20	80%; 1000
Ref. ¹⁸	DTT	2 M MnSO ₄ + 2 M H ₂ SO ₄	100, 10	92%; 4000
Ref. ¹⁹	TABQ-COF	0.5 M H ₂ SO ₄	90, 50	≈ 100%; 7500

Table S2. Comparison of electronic conductivity of organic electrode materials.

References	Organic material	Electronic conductivity (S cm ⁻¹)
This work	PTO-NH₂	2.68×10 ⁻⁸
Ref. ¹	PTO	2.08×10 ⁻⁸
Ref. ²⁰	PANI	5×10 ⁻¹¹
Ref. ²¹	PBQS	6.51×10 ⁻⁹
Ref. ²²	PAQS	< 1×10 ⁻¹¹
Ref. ²³	PDMcT	5.9×10 ⁻¹³
Ref. ²⁴	2Q	1.78×10 ⁻¹³
Ref. ²⁵	phenazine	< 1×10 ⁻¹⁴

References

1. S. Zheng, D. Shi, T. Sun, L. Zhang, W. Zhang, Y. Li, Z. Guo, Z. Tao and J. Chen, Hydrogen bond networks stabilized high-capacity organic cathode for lithium-ion batteries, *Angew. Chem.-Int. Edit.*, 2023, **62**, e202217710.
2. Z. Song, L. Miao, Y. Lv, L. Gan and M. Liu, NH₄⁺ charge carrier coordinated H-bonded organic small molecule for fast and superstable rechargeable zinc batteries, *Angew. Chem.-Int. Edit.*, 2023, **62**, e202309446.
3. Z. Chen, H. Su, P. Sun, P. Bai, J. Yang, M. Li, Y. Deng, Y. Li, Y. Gen and Y. Xu, A nitroaromatic cathode with an ultrahigh energy density based on six-electron reaction per nitro group for lithium batteries, *Proc. Natl. Acad. Sci. U. S. A.*, 2022, **119**, e2116775119.
4. M. J. Frisch, G. W. Trucks, H. B. Schlegel, G. E. Scuseria, M. A. Robb, J. R. Cheeseman, G. Scalmani, V. Barone, G. A. Petersson, H. Nakatsuji, X. Li, M. Caricato, A. V. Marenich, J. Bloino, B. G. Janesko, R. Gomperts, B. Mennucci, H. P. Hratchian, J. V. Ortiz, A. F. Izmaylov, J. L. Sonnenberg, Williams, F. Ding, F. Lipparini, F. Egidi, J. Goings, B. Peng, A. Petrone, T. Henderson, D. Ranasinghe, V. G. Zakrzewski, J. Gao, N. Rega, G. Zheng, W. Liang, M. Hada, M. Ehara, K. Toyota, R. Fukuda, J. Hasegawa, M. Ishida, T. Nakajima, Y. Honda, O. Kitao, H. Nakai, T. Vreven, K. Throssell, J. A. Montgomery Jr., J. E. Peralta, F. Ogliaro, M. J. Bearpark, J. J. Heyd, E. N. Brothers, K. N. Kudin, V. N. Staroverov, T. A. Keith, R. Kobayashi, J. Normand, K. Raghavachari, A. P. Rendell, J. C. Burant, S. S. Iyengar, J. Tomasi, M. Cossi, J. M. Millam, M. Klene, C. Adamo, R. Cammi, J. W. Ochterski, R. L. Martin, K. Morokuma, O. Farkas, J. B. Foresman and D. J. Fox, *Gaussian 16 Revision. A.03*, Gaussian Inc., Wallingford, CT, 2016.
5. Lee, Yang and Parr, Development of the Colle-Salvetti correlation-energy formula into a functional of the electron density, *Phys. Rev. B*, 1988, **37**, 785-789.
6. Becke and D. Axel, Density-functional thermochemistry. III. The role of exact exchange, *J. Chem. Phys.*, 1993, **98**, 5648-5652.
7. S. H. Vosko, L. Wilk and M. Nusair, Accurate spin-dependent electron liquid correlation energies for local spin density calculations: a critical analysis, *Can. J. Phys.*, 1980, **58**, 1200-1211.
8. S. Grimme, S. Ehrlich and L. Goerigk, Effect of the Damping Function in Dispersion Corrected Density Functional Theory, *J. Comput. Chem.*, 2011, **32**, 1456-1465.
9. T. Lu and F. Chen, Multiwfn: A multifunctional wavefunction analyzer, *J. Comput. Chem.*, 2012, **33**, 580-592.
10. W. Humphrey, A. Dalke and K. Schulten, VMD: Visual molecular dynamics, *J. Mol. Graph.*, 1996, **14**, 33-38.
11. J. Qiao, M. Qin, Y. Shen, J. Cao, Z. Chen and J. Xu, A rechargeable aqueous proton battery based on a dipyrrophenazine anode and an indium hexacyanoferrate cathode, *Chem. Commun.*, 2021, **57**, 4307-4310.
12. M. Shi, J. He, Y. Zhao, L. Zhao, K. Dai and C. Yan, In-situ Raman investigation and application of phenazine-based organic electrode in aqueous proton batteries, *Mater. Des.*, 2022, **222**, 111043.

13. M. Zhu, L. Zhao, Q. Ran, Y. Zhang, R. Peng, G. Lu, X. Jia, D. Chao and C. Wang, Bioinspired catechol-grafting pedot cathode for an all-polymer aqueous proton battery with high voltage and outstanding rate capacity, *Adv. Sci.*, 2022, **9**, 2103896.
14. Y. Dai, X. Yan, J. Zhang, C. Wu, Q. Guo, J. Luo, M. Hu and J. Yang, High-capacity proton battery based on π -conjugated N-containing organic compound, *Electrochim. Acta*, 2023, **442**, 141870.
15. M. Shi, R. Wang, L. Li, N. Chen, P. Xiao, C. Yan and X. Yan, Redox-active polymer integrated with Mxene for ultra-stable and fast aqueous proton storage, *Adv. Funct. Mater.*, 2023, **33**, 2209777.
16. X. Wang, J. Zhou and W. Tang, Poly(dithieno 3,2-*b*:2',3'-*d* pyrrole) twisting redox pendants enabling high current durability in all-organic proton battery, *Energy Storage Mater.*, 2021, **36**, 1-9.
17. G. Zhao, X. Yan, Y. Dai, J. Xiong, Q. Zhao, X. Wang, H. Yu, J. Gao, N. Zhang, M. Hu and J. Yang, Searching high-potential dihydroxynaphthalene cathode for rocking-chair all-organic aqueous proton batteries, *Small*, 2024, **20**, 2306071.
18. Y. Wang, C. Wang, W. Wang, Y. Zhang, Z. Guo, J. Huang, L. Yan, J. Ma and Y. Wang, Organic hydronium-ion battery with ultralong life, *ACS Energy Lett.*, 2023, **8**, 1390-1396.
19. Q. Zhao, Y. Ni, Y. Lu, W. Xie, H. Li, Z. Yan, K. Zhang, Y. Li and J. Chen, Dual active site covalent organic framework anode enables stable aqueous proton batteries, *Angew. Chem.-Int. Edit.*, 2025. DOI: 10.1002/anie.202424025.
20. H. Shi, Y. Ye, K. Liu, Y. Song and X. Sun, A long-cycle-life self-doped polyaniline cathode for rechargeable aqueous zinc batteries, *Angew. Chem.-Int. Edit.*, 2018, **57**, 16359-16363.
21. X. Yu, K. Zhou, C. Liu, J. Li, J. Ma, L. Yan, Z. Guo and Y. Wang, Activating organic electrode for zinc batteries via adjusting solvation structure of Zn ions, *Angew. Chem.-Int. Edit.*, 2025. DOI: 10.1002/anie.202501359.
22. Z. Song, T. Xu, M. L. Gordin, Y. Jiang, I. T. Bae, Q. Xiao, H. Zhan, J. Liu and D. Wang, Polymer-graphene nanocomposites as ultrafast-charge and -discharge cathodes for rechargeable lithium batteries, *Nano Lett.*, 2012, **12**, 2205-2211.
23. J. Li, H. Zhan and Y. Zhou, Synthesis and electrochemical properties of polypyrrole-coated poly(2,5-dimercapto-1,3,4-thiadiazole), *Electrochem. Commun.*, 2003, **5**, 555-560.
24. C. Peng, G. Ning, J. Su, G. Zhong, W. Tang, B. Tian, C. Su, D. Yu, L. Zu, J. Yang, M. Ng, Y. Hu, Y. Yang, M. Armand and K. P. Loh, Reversible multi-electron redox chemistry of π -conjugated N-containing heteroaromatic molecule-based organic cathodes, *Nat. Energy*, 2017, **2**, 17074.
25. S. Lee, J. Hong, S. Jung, K. Ku, G. Kwon, W. Seong, H. Kim, G. Yoon, I. Kang, K. Hong, H. Jang and K. Kang, Charge-transfer complexes for high-power organic rechargeable batteries, *Energy Storage Mater.*, 2019, **20**, 462-469.